# The influence of historical sea-surface temperature patterns on regional precipitation trends

Jaydeep R. Pillai* (Department of Atmospheric and Climate Science, University of Washington, Seattle, WA ; jpillai@uw.edu)

Kyle C. Armour (Department of Atmospheric and Climate Science & School of Oceanography, University of Washington, Seattle, WA ; karmour@uw.edu)

David S. Battisti (Department of Atmospheric and Climate Science, University of Washington, Seattle, WA ; battisti@uw.edu)

*Corresponding Author

The following is a non-peer reviewed preprint submitted to EarthArXiv. This article was submitted to Journal of Climate for review.

# The influence of historical sea-surface temperature patterns on regional precipitation trends

Jaydeep R. Pillai[1] , Kyle C. Armour[1,2], and David S. Battisti[1]

[1]*Department of Atmospheric and Climate Science, University of Washington, Seattle, Washington*

[2]*School of Oceanography, University of Washington, Seattle, Washington*

*Corresponding author*: Jaydeep R. Pillai, jpillai@uw.edu

ABSTRACT: State-of-the-art coupled global climate models (GCMs) fail to simulate key features of observed seasonal precipitation trends since 1980, including drying of the southwestern US, the southeastern US, East Africa, and subtropical South America, as well as wetting of the Maritime Continent and the Amazon. They also fail to simulate the sea-level pressure (SLP) trends since 1980 associated with a poleward shift of the North Pacific storm track in the mid-latitudes and a strengthened Pacific Walker Circulation. We show that state-of-the-art atmosphere-only climate model ensembles driven by observed sea-surface temperatures (SSTs) simulate historical precipitation and SLP trends that are more similar to those observed in the regions noted above, suggesting that the observed pattern of SST changes has shaped regional precipitation and SLP trends. Analysis of the coupled and atmosphere-only model ensembles reveals that multidecadal SST patterns similar to those of the interannual El-Niño Southern Oscillation are responsible for some of the regional trends simulated. The tropical Pacific zonal SST gradient is found to have substantially contributed to observed drying over the southwestern and southeastern US, signifying a key role for tropical Pacific warming patterns in future precipitation trends in these regions.

## 1. Introduction

Global warming due to increasing concentrations of greenhouse gases is expected to produce substantial changes in the hydrological cycle around the world, affecting the regional distribution of precipitation (Douville et al. 2021) with major implications for snow cover (Adam et al. 2009), terrestrial and marine ecosystems (Weltzin et al. 2003; Doney et al. 2012), water availability (Konapala et al. 2020), and soil moisture (Seneviratne et al. 2010). Substantial seasonal precipitation trends have been observed and studied over recent decades including in the southwestern United States (US; e.g. Lehner et al. 2018; Seager and Hoerling 2014; Cayan et al. 2010; Williams et al. 2022), the southeastern US (Easterling et al. 2017; Qian et al. 2024), the Amazon Rainforest (Gloor et al. 2015; Almeida et al. 2016; Moreira et al. 2024), East Africa (Rowell et al. 2015; Gebrechorkos et al. 2019), and other regions.

Figure 1 (left column) illustrates the seasonal precipitation trends over the period 1979-2014 from the Global Precipitation Climatology Project (GPCP) dataset (see Section 2a for details). In the Northern Hemisphere, there have been drying trends over the southwestern and southeastern US in December-January-February (DJF) and March-April-May (MAM), a drying trend in East Africa in MAM, a wetting trend over the Maritime Continent during MAM, and wetting trends over the Sahel region in June-July-August (JJA) and September-October-November (SON). Over the Amazon, there has been a strong wetting trend in MAM and a drying trend in SON. There has also been a drying trend in subtropical South America during MAM.

Figure 1 (left column) also illustrates seasonal trends in sea-level pressure (SLP; black contours) calculated from a state-of-the-art atmospheric reanalysis (ECMWF ERA5; Hersbach et al. 2020) over the same period (see Section 2a). In mid-latitudes, trends in SLP reveal changes in the average position of the storm tracks that bring precipitation to land regions (Trenberth et al. 1998). In the tropics, trends in SLP reveal changes in the areas of deep convection and weak subsidence, corresponding to regions of strong and weak precipitation, respectively. There has been a strong increase in SLP in the north Pacific during DJF and MAM, an increase in SLP in the south-central Pacific in SON, and a decrease in SLP in the Pacific sector of the Southern Ocean in MAM, JJA, and SON. There are also strong SLP trends in the northern and southern Atlantic Ocean during DJF and SON. Altogether, the observed patterns of precipitation and SLP changes over recent decades show large regional trends with distinct seasonality.

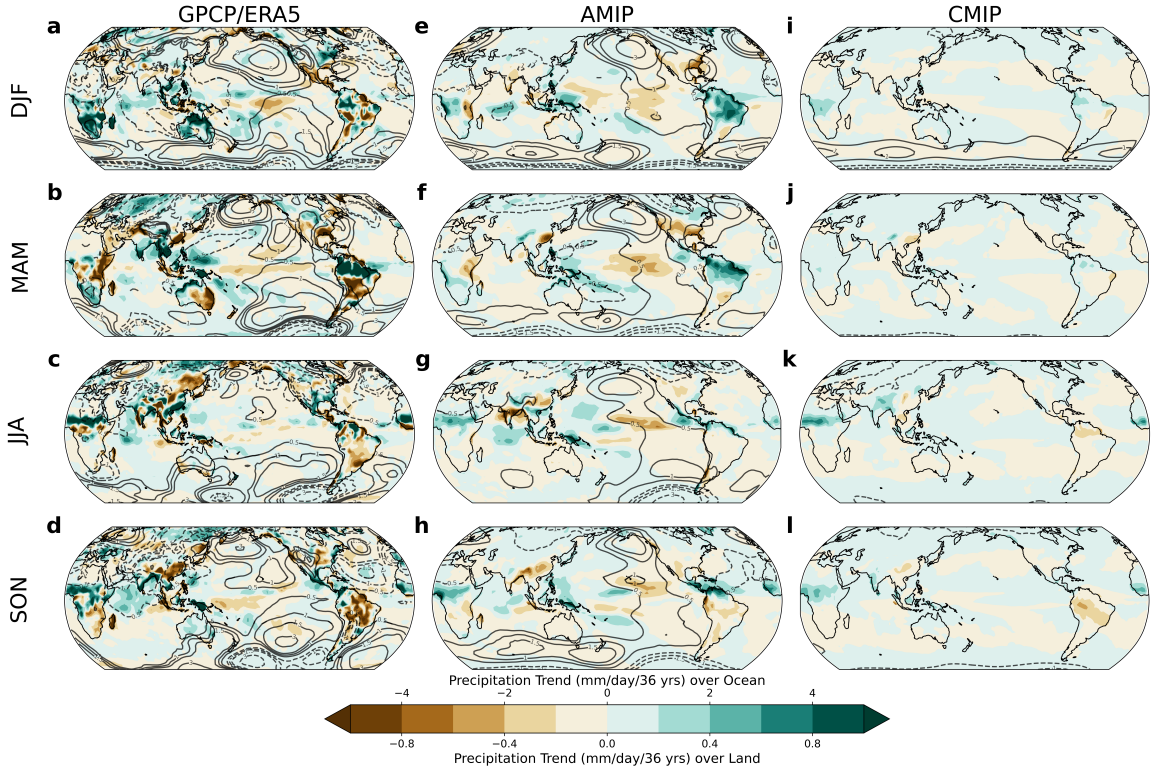


FIG. 1. Seasonal trends in precipitation and sea-level pressure (SLP) over 1979-2014 from (left, a-d) GPCPv2.3/ERA5 Reanalysis, (middle, e-h) multi-model mean AMIP simulations, and (right, i-l) multi-model mean CMIP simulations. Simulations from the same model are averaged before averaging over all model ensembles (see Eqs. 1a, 1b). Trends in precipitation over ocean and land use a different colorbar. SLP contour lines are (0.5, 1, 1.5, 3, and 5) hPa / 36 years (dashed contours are negative, zero contour is omitted).

What has driven these observed precipitation and SLP trends? Climate models can serve as a guide. Figure 1 (right column) shows 1979-2014 precipitation trends averaged over selected global climate models (restricted to those providing many ensemble members; see Section 2b and Table 1) participating in phases 5 and 6 of the Coupled Model Intercomparison Project (CMIP5, Taylor et al. 2012; CMIP6, Eyring et al. 2016). These precipitation trends represent the forced response of the fully-coupled (CMIP) models to historical changes in greenhouse gases and other forcing agents over the same period as the observations. The CMIP model forced response largely fails to reproduce observed trends in precipitation in many regions and seasons, even simulating an incorrect sign of trends in some regions, such as in the southeastern US during DJF and MAM, East

Africa during MAM, and subtropical South America during MAM. Likewise, the CMIP forced response fails to reproduce the observed trends in SLP in the same regions and seasons.

The inability of the CMIP multimodel mean to reproduce many of the observed precipitation and SLP trend patterns does not necessarily indicate that the models' forced response is wrong, given that observations reflect only a single realization of internal climate variability. Observations of sea-surface temperature (SST) trend patterns have been shown to differ substantially from the forced SST trends simulated by CMIP models (Wills et al. 2022). In particular, observations have shown a large-scale cooling trend in the central-eastern Pacific Ocean and a warming trend in the western tropical Pacific Ocean in all seasons – a strengthening of the east-west (zonal) equatorial SST gradient that broadly resembles a trend toward La Niña-like conditions (Fig. 2). In turn, atmospheric teleconnections emanating from the tropical Pacific have contributed to a poleward shift of the storm tracks and thus to changes in SLP and precipitation patterns. Indeed, the observed SLP and precipitation trends over North America have been linked to the observed pattern of tropical SST trends (Seager and Hoerling 2014; Lehner et al. 2018; Siler et al. 2019; Qiu et al. 2024), implying that the inability of the CMIP model forced response to capture observed SLP and precipitation trends in those regions may be traced to their inability to capture the unique observed tropical SST trend patterns (e.g., Wills et al. 2022). The question arises: can CMIP model biases in SLP and precipitation trends in other regions also be traced to their biases in tropical SST trend patterns?

Here, we study the global influence of historical SST trend patterns on regional precipitation trends since 1979. To do so, we compare precipitation and SLP trends simulated using fully-coupled CMIP models with both observations and trends simulated as part of the Atmospheric Model Intercomparison Project (AMIP; Taylor et al. 2012; Eyring et al. 2016), wherein atmospheric model simulations are performed using the same historical radiative forcing as in the fully-coupled CMIP models, but with observed SSTs and sea-ice concentrations prescribed. Hoerling et al. (2010) conducted a similar study using CMIP3 models, however the AMIP models they analyzed did not include time-varying radiative forcing.

Figure 2 shows the multimodel mean SST trends for AMIP (left column) and CMIP (middle column) for the same set of models over 1979-2014. The AMIP simulations (with SSTs prescribed from observations) show broad cooling in the central-eastern Pacific and warming in the western

Pacific in all seasons. The AMIP simulations also show cooling in the Southern Ocean and warming throughout the rest of the oceans. In contrast, the CMIP models show more uniform warming across all ocean basins. The right column of Fig. 2 shows the difference between CMIP-simulated and AMIP (observed) SST trends, highlighting large discrepancies throughout the Pacific and Southern Oceans.

The middle column of Fig. 1 (e-h) shows the precipitation and SLP trends in the AMIP simulations. The AMIP simulations show broad improvement in simulating observed regional precipitation and SLP trends compared to the CMIP forced response. In the Northern Hemisphere, the AMIP simulations capture the observed drying trends in the southwestern and southeastern US during DJF and MAM, the drying trend in East Africa during MAM, the wetting trend over the Maritime Continent during DJF, MAM, and SON, and the wetting trend over the Sahel during SON. In the Southern Hemisphere, the AMIP models capture the observed wetting trend over the Amazon in MAM and the drying trend over the Amazon during SON. The AMIP SLP trends also better resemble those from the ERA5 reanalysis, with large positive trends in the North Pacific during DJF and MAM as well as negative trends in the Southern Ocean during DJF, JJA, and SON.

Given that the AMIP and CMIP models are driven by identical radiative forcing, and differ only in their SST patterns, these findings (Figs. 1 and 2) suggest that the unique pattern of observed SST trends has indeed contributed to the observed trends in regional precipitation and SLP in several seasons and regions around the world. However, key questions remain: 1) How well do AMIP simulations capture observed precipitation trends? 2) Are the mechanisms linking SST trend patterns to precipitation and SLP trends over recent decades the same as those linking SST patterns to precipitation and SLP changes on interannual timescales (e.g., mediated by the well-understood atmospheric dynamics associated with the El Niño Southern Oscillation, ENSO)? 3) What role does the tropical Pacific zonal SST gradient in particular play in shaping precipitation trends, compared to SST trends in other ocean basins? Answering these questions is the aim of this study, with implications for understanding historical precipitation trends and predicting precipitation changes as the SST pattern evolves in the future.

The outline of this paper is as follows: Section 2 describes the datasets and methods used. Section 3 describes the analysis and results in five parts: the criteria for regional analysis (Section 3a); observed and modeled SST/sea-level-pressure/precipitation teleconnections on interannual

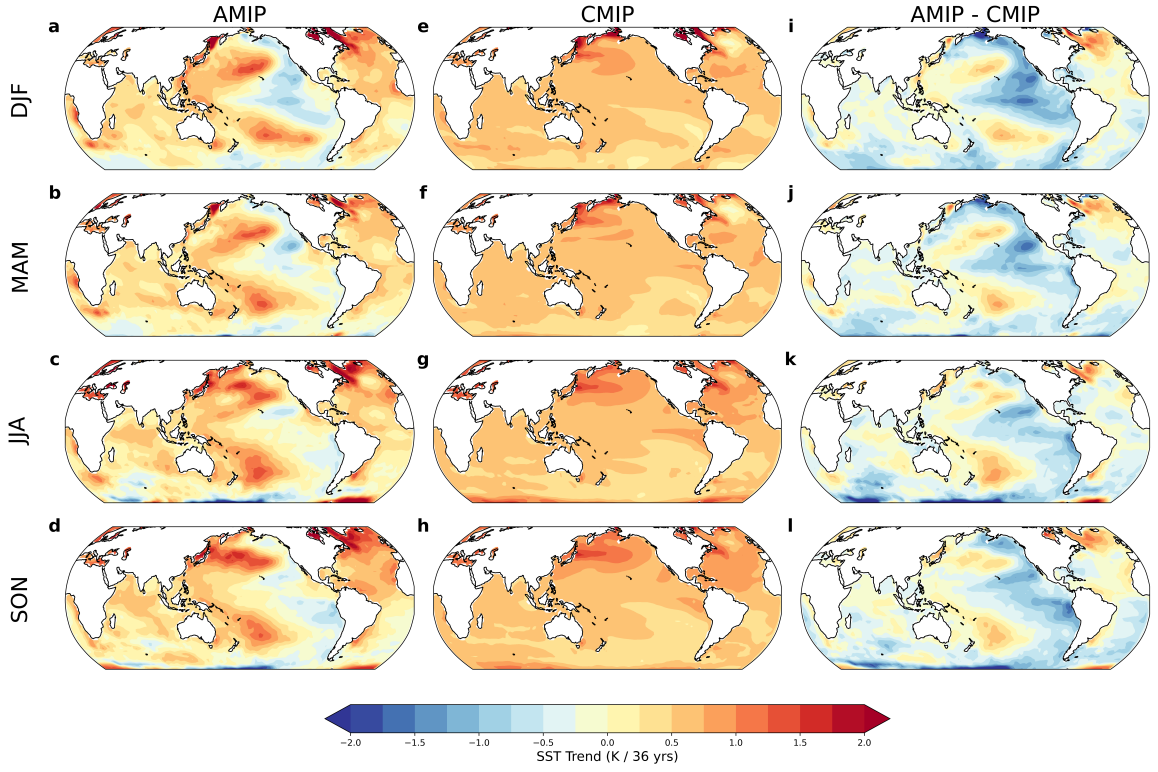


FIG. 2. Seasonal trends in sea-surface temperature (SST) over 1979-2014 from (left, a-d) observations used to force the AMIP simulations, (middle, e-h) multi-model mean CMIP simulations, and (right, i-l) the difference between AMIP and CMIP simulations. Simulations from the same CMIP model are averaged before averaging over all model ensembles (see Eqs. 1a, 1b).

timescales (Section 3b); an evaluation of whether teleconnections associated with interannual variability also mediate long-term precipitation and circulation trends (Section 3c); the role of the tropical Pacific zonal SST gradient in regional precipitation trends (Section 3d); and why some regions' precipitation may not be influenced by the unique pattern of observed SST trends (Section 3e). Finally, we discuss implications for future precipitation trends, with a focus on regions where the tropical Pacific has had a dominant influence on precipitation trends in recent decades.

## 2. Data & Methods

### *a. Observations and reanalysis data*

For observed precipitation, we use the Global Precipitation Climatology Project version 2.3 (GPCP, Adler et al. 2018). GPCP provides near-global coverage of precipitation by blending

observations from rain gauges and satellites since 1979. These data are monthly means with a resolution of 2.5° latitude × 2.5° longitude, and are the main observed precipitation dataset used for Sections 3a-d. In Section 3d, we compare the results with two other precipitation products: the National Oceanic and Atmospheric Administration Climate Prediction Center Merged Analysis of Precipitation (NOAA CMAP, Xie and Arkin 1997) and the Global Precipitation Climatology Centre Full Data Reanalysis (GPCC, Schneider et al. 2022). The NOAA CMAP product, much like the GPCP product, combines near-global satellite coverage with rain gauge measurements of monthly mean precipitation, starting in 1979 and continuing to the present with a resolution of 2.5° latitude × 2.5° longitude. The GPCC product is composed of weather station measurements of monthly mean precipitation from 1891 through 2019 at a resolution of 2.5° latitude × 2.5° longitude.

For SLP, we use the ECMWF Reanalysis version 5 (ERA5; Hersbach et al. 2020). These data are also monthly means from January 1979 to the present, with a resolution of 0.25° latitude × 0.25° longitude. For observed SSTs, we use the National Oceanic and Atmospheric Administration Extended Reconstruction Sea-Surface Temperature version 5 (ERSSTv5, Huang and Coauthors 2017), a 2.0 ° latitude × 2.0° longitude monthly gridded dataset extending from January 1854 to the present. We conduct our analyses over the period 1979–2014 to coincide with the start of the satellite era (1979) and the end of the most recent publicly available AMIP simulations (2014).

### *b. Climate model data*

Isolating the forced response of a climate model requires a large ensemble of simulations that can be averaged to reduce the influence of internal variability. Each ensemble member is initialized from a perturbed set of initial conditions and evolves under the same radiative forcing. For each CMIP model, we analyze the corresponding AMIP model, which is composed of the same atmosphere and land module as its CMIP counterpart. Each AMIP model ensemble is forced with the same radiative forcing as its CMIP counterpart, but has observed SSTs and sea-ice concentrations prescribed as surface boundary conditions. Individual AMIP ensemble members are also initialized from a perturbed set of initial conditions, producing an estimate of internal atmospheric variability that occurs given the same prescribed SSTs, sea-ice conditions, and radiative forcing. Averaging over the ensemble members of CMIP model large ensembles provides an estimate of the climate

| CMIP Model (members) | AMIP Model (members, End Date) | References |
|---|---|---|
| CESM1.1 (40) | CAM5-GOGA (10, 2015) | Kay et al. (2015) |
| CanESM2 (50) | CanAM4 (5, 2009) | Kirchmeier-Young et al. (2017), von Salzen et al. (2013) |
| GFDL-CM3 (20) | GFDL-CM3 AMIP (5, 2008) | Sun et al. (2018) |
| MPI-ESM-LR (100) | ECHAM6 (3, 2008) | Maher et al. (2019) |
| EC-Earth (16) | EC-Earth AMIP (1, 2008) | Hazeleger et al. (2010) |
| CESM2(CMIP6 Forcing) (50) | CAM6-GOGA (10, 2021) | Rodgers et al. (2021) |
| MIROC6 (50) | MIROC6 AMIP (10, 2014) | Tatebe et al. (2019) |
| MPI-ESM1.2-LR (50) | MPI-ESM1.2-LR AMIP (3, 2014) | Olonscheck et al. (2023) |

TABLE 1. CMIP large ensembles (and corresponding AMIP ensemble) used for analysis as well as the number of members ($N$) used within each ensemble.

response to historical forcing. Meanwhile, averaging over the ensemble members of the AMIP model ensembles provides an estimate of the climate response to historical forcing subject to the observed timeseries of SSTs and sea-ice concentrations. Table 1 outlines the CMIP and AMIP models used (8 in total), as well as the number of members constituting each ensemble.

We analyze monthly mean precipitation, SLP, and SST fields from the CMIP and AMIP *historical* forcing simulations. For models where SST data could not be found, we analyze surface temperature (model variable *TS*) data masked by land and we omit high-latitude areas under sea-ice cover. All data was downloaded from the Earth System Grid Federation (Cinquini et al. 2014) and the National Center for Atmospheric Research Climate Data Gateway (NCAR CDG). The precipitation data includes both liquid and solid phase and both convective and large-scale precipitation.

Some AMIP simulations from the CMIP5 generation of models end before December 2014. In this case, any linear trends calculated are still scaled by 36 years, and regional analysis is performed in areas where our results do not change with respect to a varying end date. For the CMIP5 (coupled) simulations of historical forcing and the CAM5-GOGA simulations (both ending in 2006), we append data from the Representative Concentration Pathways (RCP) 8.5 scenario to 2014.

### *c. Methods*

To motivate regions for the analysis of precipitation, we calculate the linear trends in 3-month-average precipitation and SLP for observations/reanalysis, AMIP ensembles, and CMIP ensembles, sliding the 3-month average every month. For the CMIP and AMIP models, we calculate the ensemble average trends as:

$$\overline{S}_j = \frac{1}{N_j} \sum_{k=1}^{N_j} S_{jk}, \tag{1a}$$

where $N_j$ is the number of ensemble members for model $j$, and $S_{jk}$ is the trend in precipitation/SLP for ensemble member $k$. We then regrid ensemble averages bilinearly to a common resolution (2.5° latitude × 2.5° longitude) before averaging over all models:

$$\langle S \rangle = \frac{1}{M} \sum_{j=1}^{M} \bar{S}_j, \tag{1b}$$

where $M = 8$ is the total number of models, and $\overline{S}_j$ is the average trend over model $j$. We calculate all subsequent ensemble and model averages using Eqs (1a, 1b). Figure 1 shows the results for meteorological seasons DJF, MAM, JJA, and SON.

We compute the difference in the modeled 3-month average trends in precipitation from the GPCP trends, and also compute the difference between the AMIP and CMIP ensembles. We normalize these differences by a measure of the spread in precipitation trends associated with intrinsic atmospheric variability, $\sigma_{AMIP}$, estimated as follows. First, we calculate the standard deviation of precipitation trend across the ensemble members of each AMIP model:

$$\sigma_j = \sqrt{\frac{1}{N_j} \sum_{k=1}^{N_j} (S_{jk} - \overline{S_j})^2}, \tag{2}$$

where $N_j$ is the number of ensemble members in a given model, $j$ is the model, $\overline{S_j}$ is the mean precipitation trend for model $j$, and $S_{jk}$ is the trend of an individual ensemble member in precipitation. We then average the $\sigma_j^2$ over all the models to obtain $\sigma_{AMIP}$:

$$\sigma_{AMIP} = \sqrt{\frac{1}{M} \sum_{j=1}^{M} \sigma_j^2}. \tag{3}$$

$\sigma_{AMIP}$ represents the the standard deviation in precipitation trends due to internal atmospheric variability when SSTs and sea ice are prescribed (i.e., that arising from chaotic atmospheric motions). $\sigma_{AMIP}$ provides a measure of how closely we could ever expect climate model simulations to capture observed precipitation trends, given that those trends reflect a single realization of

intrinsic atmospheric variability. When differences between modeled and observed trends are much larger than $\sigma_{AMIP}$, those differences cannot be attributed to internal atmospheric variability and thus reflect a robust difference. However, when differences between modeled and observed trends are smaller than $\sigma_{AMIP}$, then those differences might have arisen from intrinsic atmospheric variability in the observations, and we thus regard them as in agreement.

## 3. Analysis

### *a. Identifying regions and seasons of interest based on observed and simulated precipitation trends*

Figure 1 showed precipitation trends from observations (GPCP), AMIP models, and CMIP models. Figure 3 shows the difference between GPCP, AMIP, and CMIP trends, normalized by $\sigma_{AMIP}$ for each season to illustrate where the differences are large compared to trends that can occur due to intrinsic atmospheric variablity alone, which we use as a measure of significance. The right column of Fig. 3 shows differences in precipitation trends between AMIP and CMIP models. Because AMIP and CMIP models are driven by identical historical radiative forcing, any large differences in their precipitation trends can be attributed to differences between the observed and CMIP-simulated patterns of SST trends.

#### 1) Identifying regions of interest

We highlight eight land regions of interest with either red or dashed magenta boxes (Fig. 3). Red boxes indicate regions where 1) CMIP models show geographically coherent differences from the observed precipitation trends, 2) AMIP models show a substantially smaller bias than the CMIP models compared to the observed trends, and 3) AMIP models correctly simulate the sign of the observed trend. The red boxes thus illustrate regions where the observed precipitation trend is in large part explained by the unique pattern of SST trends observed over recent decades, rather than by the forced response to historical forcing.

For example, in the southwestern US the CMIP model mean shows large and widespread precipitation trend biases during MAM, with the CMIP models simulating a weak drying trend that is over $2.0\sigma_{AMIP}$ from the observed strong drying trend (Figs. 3b and 1b). However, AMIP models simulate a strong drying trend that is in good agreement with the observed trend in this region (Fig. 3f). The difference between AMIP and CMIP responses (Fig. 3j) provides a measure of how the

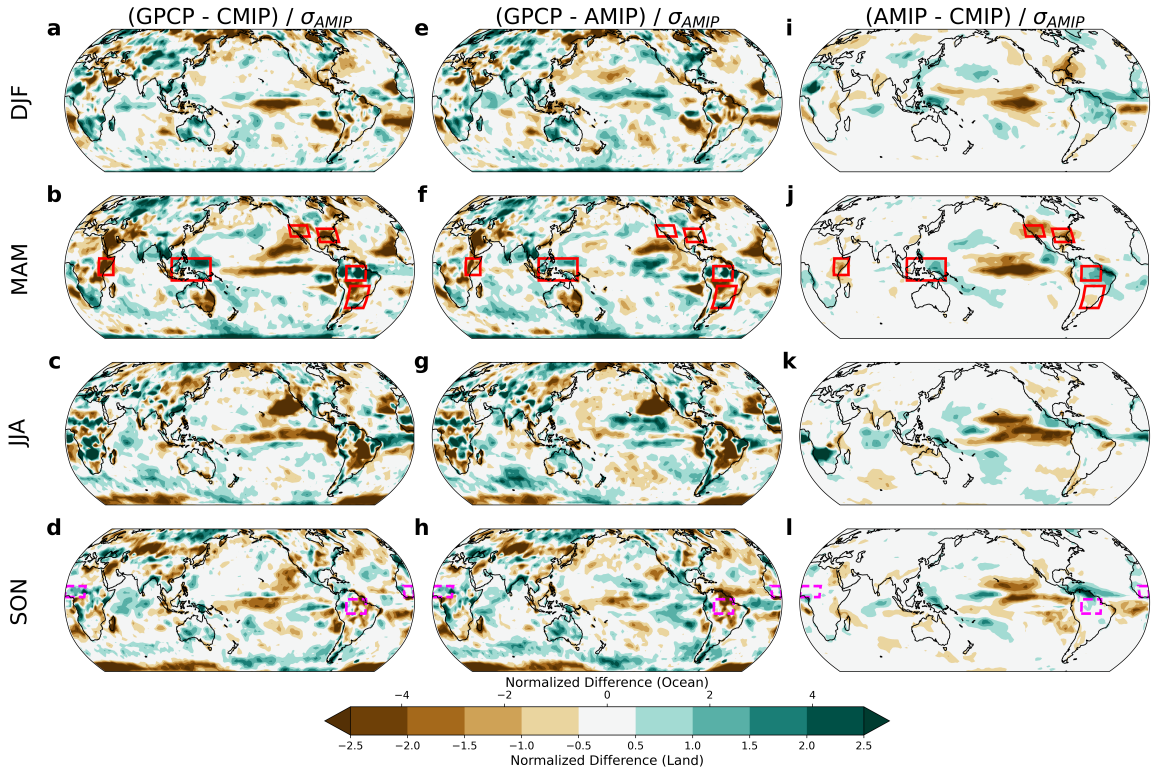


239 FIG. 3. Seasonal differences in precipitation trends over 1979-2014 normalized by the average standard
240 deviation of precipitation trends in the AMIP ensembles ($\sigma_{AMIP}$). Comparing (left) GPCP to CMIP model
241 forced response, (middle) GPCP to AMIP model forced response, and (right) the difference between AMIP
242 and CMIP model forced responses. Darker colors illustrate where differences are large compared to internal
243 atmospheric variability, while white illustrates where differences are small compared to internal atmospheric
244 variability. Red boxes highlight regions where AMIP models show substantially smaller biases in the simulated
245 trend and simulate the correct sign of the observed change, indicating that the observed precipitation trend
246 is in part due to observed SST trends that differ from the forced CMIP SST trend. Magenta dashed boxes
247 indicate regions in seasons where the CMIP and AMIP models both capture the observed precipitation trend,
248 indicating that the difference between observed and CMIP-simulated SST trends does not significantly influence
249 precipitation trends there.

237 unique observed SST pattern has influenced precipitation trends: it has contributed substantially
238 to the strong drying trend over the southwest US in MAM.

250 A similar story can be seen in other regions as well. In the southeastern US in MAM, the
251 CMIP models simulate a wetting trend that is over $2.5\sigma_{AMIP}$ from the observed strong drying

trend (Figs. 3b and 1b), while AMIP models simulate a drying that is in much better agreement with observations (Figs. 3b, f). In East Africa during MAM, the CMIP models simulate a weak wetting trend that is over $2.5\sigma_{AMIP}$ from the observed strong drying trend (Figs. 3b and 1b), and AMIP models simulate a drying trend that is in better agreement with observations, except over high-elevation regions (Fig. 3f). Over the Maritime Continent, the CMIP models simulate a weak precipitation trend that is $2.0\sigma_{AMIP}$ from the observed wetting trend in MAM, while AMIP models simulate a wetting trend that is in good agreement with observations (Fig. 3f). In South America over the Amazon Rainforest during MAM, the CMIP models simulate a weak drying trend that is over $2.5\sigma_{AMIP}$ from the observed wetting trend (Figs. 3b and 1b,j), while AMIP models simulate a wetting trend that is in better agreement with observations (Fig. 3f). In subtropical South America during MAM the CMIP models simulate a weak wetting trend that is around $2.0\sigma_{AMIP}$ from the observed drying trend (Figs. 3b and 1b), while AMIP models simulate a drying trend that is improved compared to observations, but still biased by $1.5\sigma_{AMIP}$ (Fig. 1f). While the difference between the AMIP and CMIP simulated trend in subtropical South America is small, adjusting the seasons (see Section 3a(2)) magnifies the difference and justifies our analysis of this region. In each of these regions, the difference between AMIP and CMIP responses suggests that the unique observed SST trend pattern has played a key role in the observed MAM precipitation trends (Fig. 3j).

In contrast, dashed magenta boxes on Fig. 3 highlight regions where both the CMIP and AMIP models simulate precipitation trends that are similar in magnitude and sign to the observed trend. In these regions, processes other than the difference between the observed and CMIP-simulated SST patterns dominate the precipitation trend, such as the response to the common radiative forcing prescribed in both CMIP and AMIP models. We analyze two equatorial regions within the same season (SON) where this occurs: the Sahel and the Amazon. In the Sahel, both AMIP and CMIP models simulate wetting trends similar to those observed. Normalized differences (Fig. 3l) indicate that the AMIP and CMIP models agree on the magnitude of simulated wetting. In the Amazon, AMIP and CMIP models simulate the observed drying trend, with the CMIP models simulating a stronger trend than the AMIP models. In these two regions, the similarity between AMIP and CMIP responses suggests that the unique observed SST trend pattern has not played a role in the observed SON precipitation trends (Fig. 3l).

Additional regions also show large normalized differences between the CMIP and AMIP simulations (right column of Fig. 3). However, we choose not to analyze these regions because (i) the magnitude of the trend differences between observations, CMIP models, and AMIP models are small, such is the case for the southern portion of Africa during JJA, or (ii) the observed trends are not robust with respect to a varying end date, such is the case with the Maritime Continent during SON and DJF. In the analysis that follows, we focus on the eight (red and magenta boxed) regions in Fig. 3.

### 2) Identifying seasons of interest

| Location | Months | Trend (mm/day/36 yrs) | SSTs Matter? (Fig. 3) | tropical Pacific $SST_{W-E}$ Matters? (Fig. 7) |
|---|---|---|---|---|
| Southwestern United States | JFMA | -0.52 | ✓ | ✓ |
| Southeastern United States | JFMA | -0.78 | ✓ | ✓ |
| East Africa | MAM | -0.90 | ✓ | × |
| Maritime Continent | MAM | 1.41 | ✓ | × |
| Subtropical South America | AMJ | -0.31 | ✓ | × |
| Amazon | FMAM | 1.28 | ✓ | × |
| Amazon | ASON | -0.89 | See Section 3e | × |
| Sahel | ASON | 0.40 | See Section 3e | × |

Table 2. Locations and seasons analyzed for this study, along with the observed area-averaged trend in precipitation for 1979-2014 (from GPCPv2.3). Checkmarks indicate whether the global pattern of SST trends or the tropical Pacific zonal SST gradient trend influence the precipitation trend in that region.

For each of the regions highlighted in Section 3a(1), we broaden the seasons of interest by calculating sliding 3-month average (DJF, JFM, FMA, ... etc.) normalized differences in precipitation trends. Starting from the meteorological seasons highlighted above in Section 3a, we include neighboring months that strengthen the observed precipitation trends while excluding months that weaken trends. For example, in the southwestern US during MAM, we remove May since it diminishes the drying signal, while adding January and February since they contribute to a stronger drying over the 36-year period. Table 2 lists the broadened seasonal average analyzed for each region in the rest of the analysis and also summarizes whether the global trend pattern in SST

and the trend in the tropical Pacific zonal SST gradient contributed to the long-term trends in precipitation (Section 3d).

*b. The SST-precipitation relationship on interannual timescales*

Figure 1 and the red boxes in 3 show where AMIP models, given the observed SST trend pattern, simulate improved precipitation trends in key regions and seasons compared to CMIP models. Previous literature (Seager and Hoerling 2014, Lehner et al. 2018, Siler et al. 2019, Qiu et al. 2024) suggests that tropical SSTs are important in driving some of the regional trends. Here we explore which SST patterns are connected to precipitation and SLP changes for each of our regions and seasons of interest on the interannual timescale in both observations and models. This analysis will allow us to evaluate how well models simulate observed atmospheric teleconnections, and provide context for why model simulations may or may not capture observed trends in precipitation and atmospheric circulation in Section 3c.

To study the links between SSTs, SLP, and regional precipitation on interannual timescales, we linearly detrend the time series of each field over 1979-2014 for observations, AMIP, and CMIP models. For each AMIP model, we concatenate detrended ensemble members together into one time series. The same is done for each CMIP model. We then spatially average precipitation over each region of interest (see Table 2) and normalize the precipitation by its standard deviation over the time series. We then regress the SST/SLP at each point against the regionally averaged normalized precipitation. We apply a two-tailed Student's $t$-test to determine whether the regression coefficient at each gridpoint is significantly different from zero, at a level $p<0.1$. The regression from each model is then bilinearly regridded to a common grid (2.5° latitude × 2.5° longitude) and averaged across the 8 models. Gridpoints where fewer than 5 models have regressions that are statistically significant are stippled. Figure 4 shows the above regression of SST and SLP anomalies in normalized regional precipitation. Regression values are scaled by -1, such that SST/SLP regression values are associated with negative precipitation anomalies in the boxed region.

For observations (left column of Fig. 4), the importance of the tropical Pacific for many regions' precipitation reflects well understood ENSO teleconnections (Ropelewski and Halpert 1987; Trenberth et al. 1998; Davey et al. 2014): seasonal precipitation in the southwestern US (A1), south-

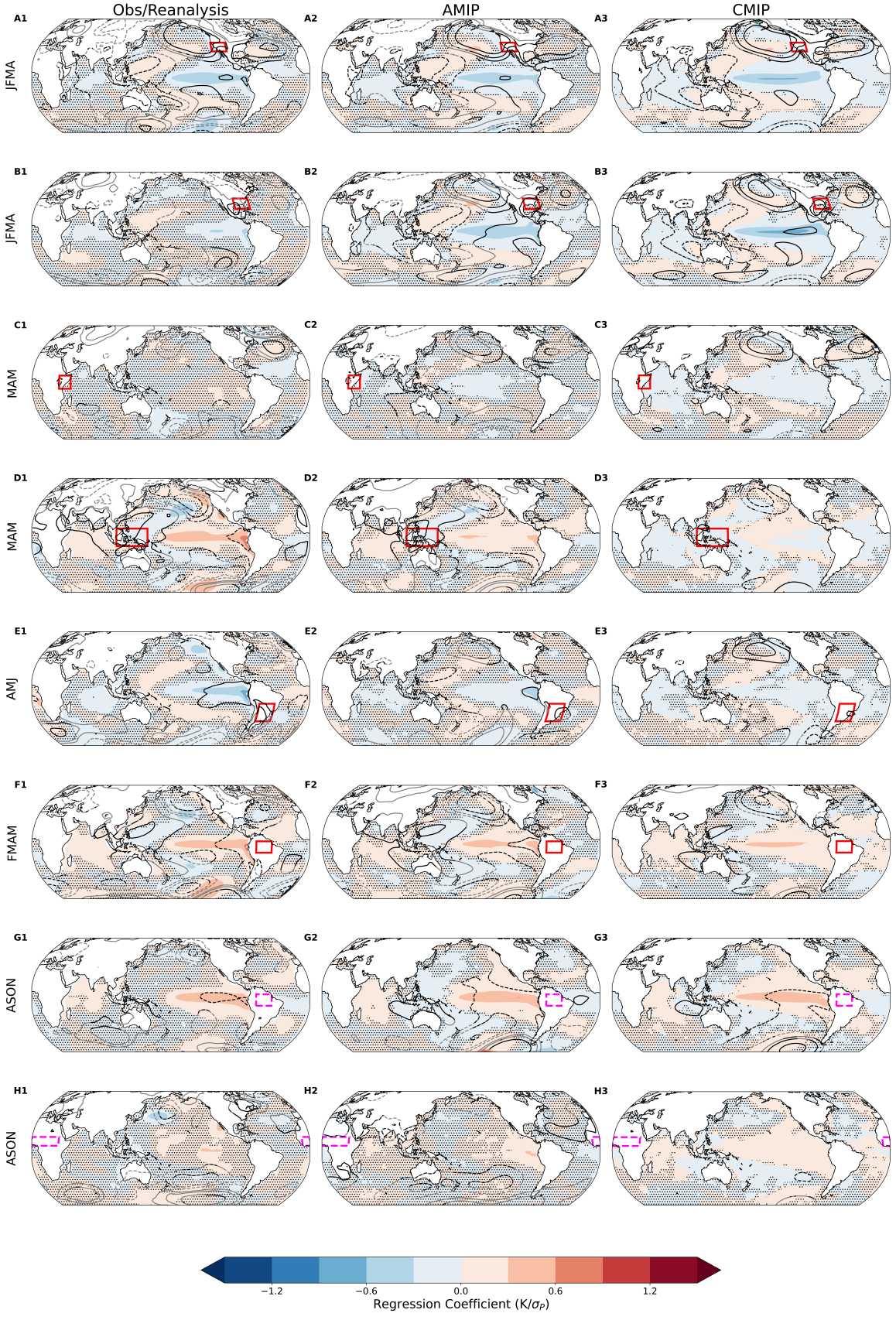
Obs/Reanalysis
AMIP
CMIP
A1
A2
A3
JFMA
B1
B2
B3
JFMA
C1
C2
C3
MAM
D1
D2
D3
MAM
E1
E2
E3
AMJ
F1
F2
F3
FMAM
G1
G2
G3
ASON
H1
H2
H3
ASON
−1.2
−0.6
0.0
0.6
1.2
Regression Coefficient (K/$\sigma_P$)

FIG. 4. Seasonal anomalies in SST and SLP regressed on normalized precipitation anomalies (averaged over the red box in each figure). Significant relationships (p <0.1) between SST anomalies and normalized precipitation are unstippled, while significant relationships between SLP anomalies and normalized precipitation are shown in black contours (otherwise grey). Regression values are scaled by -1 to facilitate comparison with the La-Niña-like SST pattern from Figure 2. SLP contours are (0.25, 0.5, 1, 2, 3, and 4) hPa / $\sigma_P$ (dashed contours are negative, zero contour is omitted).

eastern US (B1), the Maritime Continent (D1), subtropical South America (E1), and the Amazon (F1, G1) is modulated by interannual variability in tropical Pacific SST associated with ENSO. In the tropics, El-Niño conditions cause rainfall deficits in MAM in the Maritime Continent (D1) and in FMAM in the Amazon (F1). In midlatitudes, poleward propagating Rossby waves generated by anomalous tropospheric latent heating from deep convection in the tropics affect the extratropical large-scale atmospheric flow. Over the southwestern and southeastern US, La Niña causes a poleward shift in the storm tracks, indicated by the strengthening SLP over the north Pacific, reflecting fewer storms reaching these regions (Fig. 4A1). Over subtropical South America, La Niña heating anomalies cause a wave train that shifts the Southern Hemisphere storm tracks poleward, reflecting reduced precipitation reaching this region as well (Fig. 4E1; Garreaud and Battisti 1999); previous literature has also commented on the large role of interannual tropical Pacific variability on precipitation in this region (Seager et al. 2010). Comparing these observed relationships to those in the AMIP and CMIP models, we find similar SST patterns across these regions, indicating that the models simulate the observed ENSO teleconnections well.

Previous literature indicates that La-Niña-like conditions can cause weak positive precipitation anomalies in the Sahel in ASON (Fig. 4H1), and that ENSO has no effect on East African precipitation in MAM (e.g., Davey et al. 2014; Folland et al. 1991). In agreement with observations, the AMIP and CMIP ensembles show a weak relationship between precipitation anomalies in the Sahel and tropical Pacific SST (Fig. 4H1-3). In East Africa, AMIP and CMIP ensembles suggest, unlike in observations (Fig. 4C1), that La Niña conditions contribute to precipitation deficits (Fig. 4C2,3).

Figure 4 panels G1-3 show that interannual precipitation variability in the Amazon in ASON is linked to tropical Pacific SST variability in observations, AMIP models, and CMIP models. However, our results in Section 3a showed that global SSTs are not linked to long-term trends in

precipitation in this region and season. This result, which we verify in Section 3c, suggests that SST patterns are important for interannual precipitation variability in the Amazon in ASON, but are not important for multidecadal trends in precipitation.

In summary, we have shown where SSTs matter for precipitation around the world on interannual timescales. Consistent with previous studies, observations show that SST variability in the tropical Pacific affects precipitation in 5 of 8 regions considered here, indicating the importance of ENSO variability for precipitation in these regions. Our analysis also shows that AMIP and CMIP models reproduce the strong relationships observed between tropical Pacific SST, SLP, and regional precipitation anomalies in these regions.

### *c. The SST-precipitation relationship on multidecadal timescales*

The previous section established the ability of models to simulate well-understood, observed SST-precipitation teleconnections modulated by changes in atmospheric circulation on interannual timescales. In this section, we analyze the multidecadal trends (1979-2014) in the CMIP models to assess whether the observed trends could arise due to internal (unforced) SST variability, and if so, whether the processes responsible are related to trends in tropical Pacific SSTs. Previous literature has shown that SST trends can affect long-term precipitation trends, particularly in the southwestern US. For example, Lehner et al. (2018) and Siler et al. (2019) used dynamical adjustment to understand how tropical Pacific SSTs have influenced recent trends in western US precipitation and SLP, while Qiu et al. (2024) found that tropical SST trends contribute to precipitation trends over the southwestern US and Amazon regions. Kuo et al. (2023, 2025) point to the role of anthropogenic aerosols driving SST and circulation trends that influence southwestern US precipitation. Elsewhere, Rowell et al. (2015) compared CMIP and AMIP model precipitation trends and concluded that SST trends have contributed to historical drying in East Africa, but were unable to pinpoint the exact SST pattern responsible.

Here, we leverage the eight CMIP model large ensembles to evaluate whether SST and SLP trend patterns related to regional precipitation trends (1979-2014) are similar to those shown in Section 3c. For each model ensemble member, we calculate the linear trend in SLP and SST at each gridpoint and the linear trend in precipitation in each region of interest (Table 2). We then regress the gridded SST and SLP trends against the regionally-averaged precipitation trend from

each ensemble member. These results are bilinearly regridded to a common grid (2.5° latitude × 2.5° longitude) before averaging over all model ensembles. A two-tailed $t$-test is applied to test significance at level $p<0.1$; gridpoints where fewer than 5 models have regressions that are statistically significant are stippled. Results shown in Fig. 5 are scaled by -1 to reflect SST trends that are correlated with drying in the boxed region.

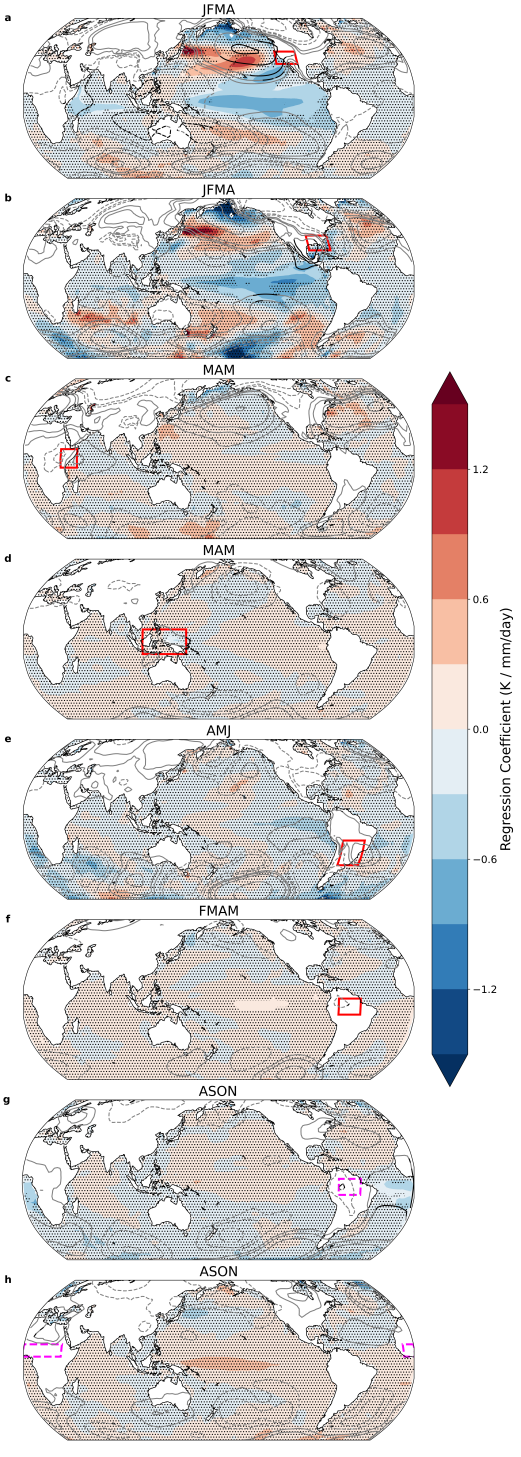
a
JFMA
b
JFMA
c
MAM
d
MAM
e
AMJ
f
FMAM
g
ASON
h
ASON
1.2
0.6
0.0
−0.6
−1.2
Regression Coefficient (K / mm/day)

FIG. 5. Model ensemble average of multidecadal trends in seasonal SST and SLP regressed against multidecadal trends in seasonal regional precipitation from each CMIP large ensemble. Trends in regional precipitation are calculated from the average over the red box in each plot. Significant relationships ($p < 0.1$) between SST trends and regional precipitation trends are unstippled. Significant relationships between SLP trends and regional precipitation trends are contoured in black (otherwise grey). SLP contours correspond to (0.25, 0.5, 1, 3, and 5) hPa/mm/day (dashed contours are negative, zero contour is ommitted). Regression values are scaled by -1 to facilitate comparison with the La-Niña-like SST pattern from Figure 2.

In the southwestern and southeastern US there is an ENSO-like relationship between SST trends in the tropical Pacific and precipitation trends in both regions (Figs. 5a,b) that is similar to the interannual relationships shown in rows A and B of Fig. 4. The negative precipitation trend in the southwestern US is also associated with a statistically significant positive SST trend in the central North Pacific (see Conclusions and Implications section). An analysis of pre-industrial control simulations from the same set of CMIP models (not shown) illustrates similar teleconnection patterns with similar model agreement, signifying that there exists robust patterns of SST trends in the tropical Pacific correlated to precipitation trends across both regions in forced and unforced simulations.

The other six regions (Maritime Continent, East Africa, subtropical South America, the Sahel, and the Amazon in both seasons) all show little to no connection between tropical Pacific SST and precipitation trends for their corresponding seasons, and this result is robust when applying a similar analysis to pre-industrial control simulations of the CMIP models (not shown). Note that our statistical constraint for significant relationships between SST, SLP and regional precipitation trends is high; relaxing this constraint from 5 or more models with regression coefficients of $p<0.1$ to 5 or more models agreeing on the *sign* regression coefficient increases the geographical area of SST and SLP trends that are associated to regional precipitation trends. However, the associated multi-model mean relationships between SST, SLP, and regional precipitation trends to these areas are still weak.

That CMIP models do not show a strong link between SST trends and precipitation trends over the Maritime Continent, subtropical South America, and East Africa is surprising, given that the ensemble-averaged trends in AMIP simulations (Fig. 3) more closely resemble observations than those from CMIP simulations. Furthermore, panels D3 and E3 in Fig. 4 demonstrate that CMIP models do simulate interannual SST–precipitation teleconnections for the Maritime Continent and subtropical South America. However, these interannual teleconnections are weaker in CMIP models than in their AMIP counterparts, which could contribute to a too-weak relationship between SSTs and precipitation on multidecadal timescales. It is also possible that the CMIP models' multidecadal SST variability never accesses the pattern of SST trends seen in observations (Wills et al. 2022), compromising the atmospheric response to these SST trends responsible for the multidecadal teleconnections to precipitation over the Maritime Continent and subtropical South

America. Other work has shown that the tropical Atlantic is responsible for multidecadal precipitation variability in subtropical South America (Seager et al. 2010), but our results do not indicate show a robust connection. In East Africa, both CMIP and AMIP models produce weak interannual SST–precipitation links that are not seen in observations (panels C1-3 of Fig. 4), suggesting that current model ensembles do not capture the SST trend patterns that contributed to observed historical drying in this region.

*d. The equatorial Pacific influence on regional precipitation trends*

We have found that tropical Pacific SST trends are linked to precipitation trends in the southwestern and southeastern US via ENSO-like teleconnections. In this section, we scale the results in Fig. 5 to determine to what extent the CMIP models would represent the observed regional precipitation trends if they had simulated the observed amplitude of the SST trend pattern in the equatorial Pacific. To do this, we define the zonal SST gradient in the equatorial Pacific following Wills et al. (2022):

$$SST_{W-E} = SST_W - SST_E, \tag{4}$$

where $SST_W$ is SST averaged over ($5°S$ - $5°N$, $110°E - 180°$) and $SST_E$ is SST averaged over ($5°S$ - $5°N$, $180°$ - $80°W$). We calculate the trend in $SST_{W-E}$ for each member of the CMIP ensemble over all of the seasons in Table 2. We also calculate the observed $SST_{W-E}$ trend in the aforementioned seasons from ERSSTv5 data. For each model, we regress the precipitation trend at each gridpoint against the $SST_{W-E}$ trend from each ensemble member, obtaining regression coefficient and intercept maps. We bilinearly regrid both maps from each model to a common grid resolution (2.5° latitude × 2.5° longitude) and then scale the regression coefficient map by the observed $SST_{W-E}$ trend before adding the intercept map. The result is a regression estimate of the precipitation trend that each model would simulate if one of its ensemble members were to accurately simulate the observed zonal SST gradient trend.

Figure 6 shows an example of this regression for area-averaged precipitation trends in the southwestern US (JFMA) in the CESM2 Large Ensemble along with precipitation trends from its corresponding AMIP ensemble. Note that the regression line fit to the CESM2 data falls within the spread of the AMIP model's simulated precipitation trends and close to the observed

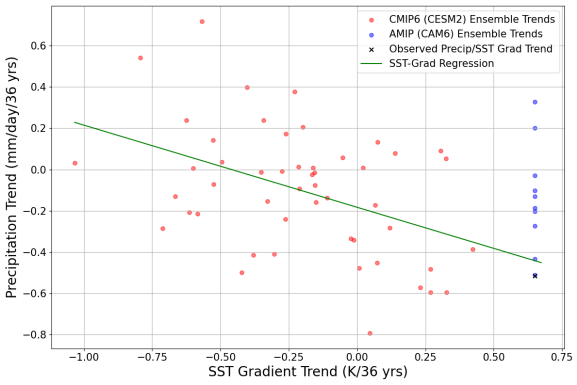


FIG. 6. Example of regressing precipitation trends against SST-gradient trends for the CESM2 Large Ensemble. Red points indicate trends from each individual ensemble member, blue points indicate trends from the corresponding AMIP model (CAM6-GOGA simulation), and the green line is the regression fit to the large ensemble, extrapolated to the observed zonal SST gradient trend. The black cross shows the observed precipitation and SST-gradient trends from GPCP and ERSSTv5 data.

precipitation trend when evaluated using the observed trend value of $SST_{W-E}$. Given that the AMIP model ensemble corresponding to CESM2 is driven by the observed zonal SST gradient trend, our regression result indicates that the equatorial Pacific zonal SST gradient trend is directly related to the precipitation trend in the southwestern US in this model.

For each region, we plot the area-averaged precipitation trend estimate (labeled SST-Grad Regression) using our regression along with the simulated CMIP and AMIP model trends in Figure 7. The observed regional precipitation trends from the GPCP, GPCC, and NOAA CMAP products are also plotted for comparison. Comparing the SST-Grad Regression box to the CMIP box for each region shows whether or not the CMIP models would be able to simulate the observed precipitation trends if they had simulated the observed zonal SST gradient in the equatorial Pacific.

Taking into account the zonal SST gradient trend helps reconcile the differences in simulated precipitation trends simulated by CMIP and AMIP models over the southwestern and southeastern US (Fig. 7a,b). In these regions, strong relationships between equatorial Pacific SST and precipitation were identified on interannual and multidecadal timescales and the results in Fig. 7 suggest equatorial Pacific SST trends are responsible for much of the drying trends in JFMA in these regions. Moreover, the estimated drying from our regression matches well with the observed

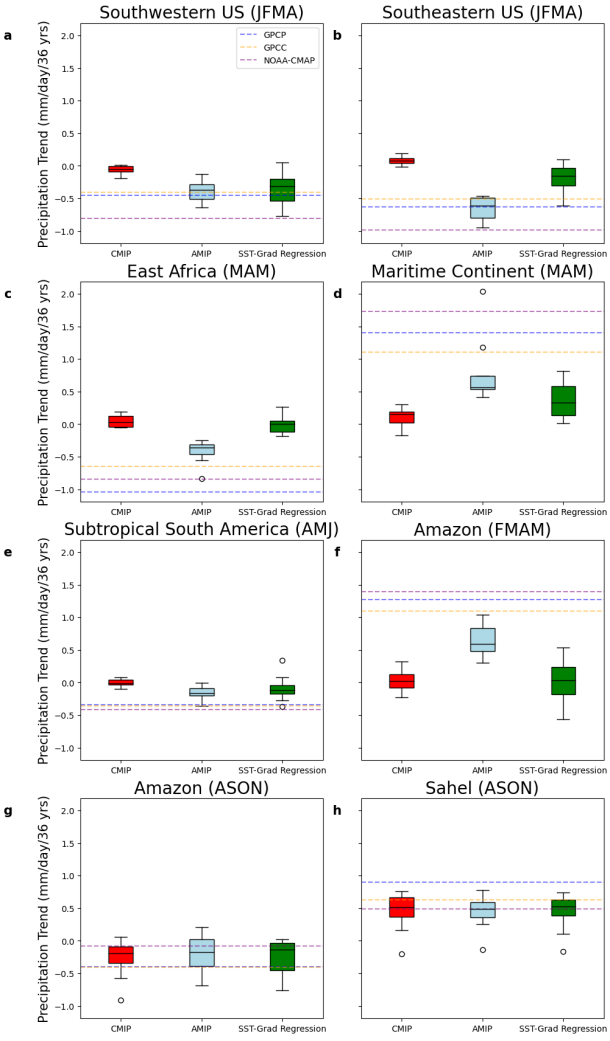


FIG. 7. Box and Whisker Plots illustrating the area-averaged trends for each region/season in Table 2 from AMIP (light blue) and CMIP (red) models, as well as the regression-estimated precipitation trend (green). The horizontal dashed lines correspond to the observed precipitation trend from three different datasets, GPCP (blue), GPCC (yellow) and NOAA CMAP (purple). The black line in each box represents the median. Circles represent flier points, which are data outside of the 1.5x inter-quartile range.

drying in the southwestern US, suggesting that the equatorial Pacific zonal SST gradient is key to understanding precipitation changes in the region.

Over the Maritime Continent (Fig. 7d), the re-scaled SST gradient trend reconciles the difference between CMIP and AMIP models' precipitation trends, but does not fully explain the observed precipitation trend. This result suggests that a process independent of the atmosphere's response to

the equatorial Pacific SST gradient contributes to the observed precipitation trend in this region. In East Africa, subtropical South America, and the Amazon (FMAM) (Figs. 7c,e,f), the re-scaled SST-gradient trend does not reconcile the differences between CMIP and AMIP models' precipitation trends, nor does it explain the observed precipitation trends in these regions. However, the AMIP models still simulate trends close to observations (Fig. 3), which indicates that SST trends outside of the equatorial Pacific may be responsible for the observed precipitation trends in these regions.

*e. Regions of agreement between AMIP and CMIP*

Two regions of interest (the Sahel and the Amazon in ASON) show little difference between AMIP and CMIP simulated precipitation trends (boxed in dashed magenta in Fig. 3). Figures 7g-h show the inter-model spread in their precipitation trends simulated by CMIP and AMIP as well as the calculation from our SST gradient regression method; all three show agreement on the weak drying trend in the Amazon Rainforest and the wetting trend in the Sahel. The shared forced response in these two regions in both the CMIP and AMIP models, despite different SST trend patterns, suggests that a common response to radiative forcing prescribed to both models is responsible for the precipitation trends. It is likely that shared tropical Atlantic SST meridional SST gradients are driving the precipitation trends in both regions.

Biasutti (2019) reviews the many hypotheses for the rebound in Sahel precipitation since the late 1970s, with the leading cause being the reduction of reflective aerosol emissions from European and North American factories. These emissions caused cooling over the North Atlantic, shifting the rain band over Western Africa southward (Folland et al. 1986; Giannini et al. 2003; Dong and Sutton 2015) away from the Sahel and led to a negative precipitation trend from 1950 to 1990. The identical aerosol emissions imposed on both CMIP and AMIP models could have led to this similar effect, as the reduction of emissions would lead to a large rebound in precipitation in the Sahel afterward as North Atlantic SSTs warm and the rain band shifts northward.

The Amazonian drying trend in ASON may also be related to SST trends. We found that negative tropical Atlantic SST trends are related to drying trends over this region and season (Fig. 5g), but the observed SST trend is weakly positive (Fig. 2d). However, the common characteristic between AMIP and CMIP SST trends in the Atlantic is a meridional SST gradient that indicates a northward

ITCZ shift over the Atlantic, which would decrease convection and rainfall over the Amazon and subsequently promote drying (Knight et al. 2008; Harris et al. 2008).

## 4. Conclusions and Implications

In this paper, we compared the precipitation responses of AMIP and CMIP model ensembles under historical forcing to observed precipitation trends around the world over 1979-2014. CMIP models fail to simulate the observed precipitation trends in most regions, while AMIP models generally produce more accurate trends. Comparing results from CMIP and AMIP models suggests that observed SST trends that are distinct from those found in the forced response of CMIP models have contributed to the observed precipitation trends in the southwestern US (JFMA, consistent with Lehner et al. 2018; Qiu et al. 2024; Kuo et al. 2025), the southeastern US (JFMA), the Maritime Continent (MAM), the Amazon (FMAM), East Africa (MAM), and subtropical South America (AMJ, consistent with Seager et al. 2010) (see Table 2).

The multidecadal JFMA drying trends in the southwestern and southeastern US showed a strong relationship to the trend in the zonal SST gradient in the equatorial Pacific, likely via teleconnections similar to those observed in interannual La Niña events. Notably, the recent multidecadal trend in southwest US winter precipitation has been reproduced in a climate model forced by observed Pacific SST (Lehner et al. 2018), with the drying primarily attributed to trends in the tropical Pacific SST (Todd et al. 2025, Supplemental Data Fig. 10). However, the latter study using the same model argues for a secondary contribution from SST trends in the North Pacific. These results suggest that teleconnections emanating from tropical Pacific SSTs are most important in setting the atmospheric circulation trends responsible for the observed drying trend over the recent historical period in the southwestern US, and to a lesser extent, the observed JFMA drying in the southeastern US.

Although the observed multidecadal SST trends (not seen in the forced response from the CMIP models) contribute to the precipitation trends in the other four regions mentioned above, those precipitation trends cannot be attributed to differences in the trends in the equatorial Pacific zonal SST gradient, but must be due to trends in SSTs elsewhere. For the wetting trends in the Maritime Continent (MAM) and the Amazon (FMAM) and the drying trend in subtropical South America (AMJ), this result is somewhat surprising because in these three regions, similarly signed

precipitation anomalies are strongly linked to La Niña events on interannual time scales that feature anomalies in the zonal SST gradients that are similar to the observed multidecadal trend. Future work may be able to leverage idealized AMIP experiments, such as TOGA (Tropical Ocean Global Atmosphere) ensembles, and ocean pacemaker ensembles to identify which specific SST patterns are most important for precipitation trends in these regions.

CMIP and AMIP models simulated similar precipitation trends in both the Sahel and Amazon (ASON); these model results suggest that the observed precipitation trends in these two regions have not been strongly affected by the unique observed SST trend pattern. Notably, while interannual tropical Pacific SST variability is known to have an effect on Amazon precipitation in ASON, there is no link to a similar relationship regarding the multidecadal drying over the same region. Our results and a review of the literature suggest that a shared tropical Atlantic SST trend response to radiative forcing common to both CMIP and AMIP models may have induced precipitation trends in both regions. Single-forcing ensembles may also provide insights into the different radiative forcings responsible for the trends in these regions.

The sign of the trend in the equatorial Pacific zonal SST gradient is expected to change in the future, eventually becoming more El-Niño-like with enhanced warming in the east Pacific (Rugenstein et al. 2020; Armour et al. 2024; Forster et al. 2021). If this projected change does occur, our regressions of precipitation trends against the equatorial Pacific SST gradient in CMIP models (Section 3d) suggest that both the southwestern and southeastern US will become wetter. These results suggest that extrapolating observed precipitation trends using the assumption that they scale with global average temperature (e.g., Kravitz et al. 2017; Kravitz and Snyder 2023; Herger et al. 2015) could lead to substantial errors in regional precipitation projections. This point is most clear for precipitation trends over the southwestern and southeastern US, where the equatorial Pacific zonal SST gradient trend has contributed substantially to observed drying. It may also be true for the Maritime Continent, the Amazon (FMAM), East Africa, and subtropical South America, where the global SST pattern was found to influence precipitation trends but the exact regional SST patterns could not be identified.

In contrast, we found that a common response to radiative forcing in both AMIP and CMIP models drives similar precipitation trends in both the Sahel and the Amazon (ASON) that agree well with the observed precipitation trend despite their differing SST trend patterns. This finding

suggests that long-term precipitation changes may scale more directly with radiative forcing or global temperature in these two regions, and may be less sensitive to uncertainties in how SST patterns may change in the future.

*Acknowledgments.* J.R.P., K.C.A., and D.S.B were supported by National Science Foundation (NSF) Award AGS-2203543. J.R.P. and D.S.B. were supported by NSF award AGS-2128409 and the Tamaki Foundation. K.C.A. was supported by a Calvin Professorship in Oceanography. We thank Robert Jnglin Wills for insightful discussions about this work.

*Data availability statement.* Model data used in the analysis can be found on the Earth System Grid Federation (https://esgf.github.io) or the NCAR Climate Data Gateway (https://www.earthsystemgrid.org). Observational data (GPCP, GPCC, NOAA CMAP, and NOAAERSSTv5 datasets) were downloaded from NOAA PSL (https://psl.noaa.gov/).

## References

Adam, J., A. Hamlet, and D. Lettenmaier, 2009: Implications of global climate change for snowmelt hydrology in the twenty-first century. *Hydrol. Process*, **23**, 962–972, https://doi.org/10.1002/hyp.7201.

Adler, R., and Coauthors, 2018: The Global Precipitation Climatology Project (GPCP) monthly analysis (new version 2.3) and a review of 2017 global precipitation. *Atmosphere*, **9**, 138, https://doi.org/10.3390/atmos9040138.

Almeida, C., J. Oliveira-Junior, R. Delgado, P. Cubo, and M. Ramos, 2016: Spatiotemporal rainfall and temperature trends throughout the Brazilian Legal Amazon, 1973-2013. *Int. J. Climatol.*, **37**, 2013–2026, https://doi.org/10.1002/joc.4831.

Armour, K., and Coauthors, 2024: Sea-surface temperature pattern effects have slowed global warming and biased warming-based constraints on climate sensitivity. *Proc. Natl. Acad. Sci. U.S.A.*, **121**, https://doi.org/10.1073/pnas.2312093121.

Biasutti, M., 2019: Rainfall trends in the African Sahel: Characteristics, processes, and causes. *WIREs Clim Change*, https://doi.org/10.1002/wcc.591.

Cayan, D., T. Das, D. Pierce, T. Barnett, M. Tyree, and A. Gershunov, 2010: Future dryness in the southwest US and the hydrology of the early 21st century drought. *Proc. Natl. Acad. Sci.*, **107**, 21 271–21 276, https://doi.org/10.1073/pnas.0912391107.

Cinquini, L., and Coauthors, 2014: The Earth System Grid Federation: An open infrastructure for access to distributed geospatial data. *Future Generation Computer Systems*, **36**, 400–417, https://doi.org/10.1016/j.future.2013.07.002.

Davey, M., A. Brookshaw, and S. Ineson, 2014: The probability of the impact of ENSO on precipitation and near-surface temperature. *Clim. Risk. Manag.*, **1**, 5–24, https://doi.org/10.1016/j.crm.2013.12.002.

Doney, S., and Coauthors, 2012: Climate change impacts on marine ecosystems. *Annu. Rev. Mar. Sci.*, **4**, 11–37, https://doi.org/10.1146/annurev-marine-041911-111611.

Dong, B., and R. Sutton, 2015: Dominant role of greenhouse-gas forcing in the recovery of Sahel rainfall. *Nature Clim Change*, **5**, 757–760, https://doi.org/10.1038/nclimate2664.

Douville, H., and Coauthors, 2021: Water cycle changes. *Climate Change 2021: The Physical Science Basis. Contribution of Working Group I to the Sixth Assessment Report of the Intergovernmental Panel on Climate Change*, V. Masson-Delmotte, P. Zhai, A. Pirani, S. Connors, C. Péan, S. Berger, N. Caud, Y. Chen, L. Goldfarb, M. Gomis, M. Huang, K. Leitzell, E. Lonnoy, J. Matthews, T. Maycock, T. Waterfield, O. Yelekçi, R. Yu, , and B. Z. (eds.), Eds., Cambridge University Press, 1055–1210, https://doi.org/10.1017/9781009157896.010.

Easterling, D., and Coauthors, 2017: Precipitation change in the United States. *Fourth National Climate Assessment*, https://doi.org/10.7930/J0H993CC.

Eyring, V., S. Bony, G. Meehl, C. Senior, B. Stevens, R. J. Stouffer, and K. Taylor, 2016: Overview of the Coupled Model Intercomparison Project Phase 6 (CMIP6) experimental design and organization. *GeoSci. Model Dev.*, **9**, 1937–1958, https://doi.org/https://doi.org/10.5194/gmd-9-1937-2016.

Folland, C., J. Owen, M. Ward, and A. Colman, 1991: Prediction of seasonal rainfall in the Sahel region using empirical and dynamical methods. *J. Forecast*, **10**, 21–56, https://doi.org/10.1002/for.3980100104.

Folland, C., T. Palmer, and D. Parker, 1986: Sahel rainfall and worldwide sea temperatures, 1901–85. *Nature*, **320**, 602–607, https://doi.org/10.1038/320602a0.

Forster, P., and Coauthors, 2021: The Earth's energy budget, climate feedbacks, and climate sensitivity. *Climate Change 2021: The Physical Science Basis. Contribution of Working Group I to the Sixth Assessment Report of the Intergovernmental Panel on Climate Change*, V. Masson-Delmotte, P. Zhai, A. Pirani, S. Connors, C. Péan, S. Berger, N. Caud, Y. Chen, L. Goldfarb, M. Gomis, M. Huang, K. Leitzell, E. Lonnoy, J. Matthews, T. Maycock, T. Waterfield, O. Yelekçi, R. Yu, , and B. Z. (eds.), Eds., Cambridge University Press, 923–1054, https://doi.org/10.1017/9781009157896.009.

Garreaud, R., and D. Battisti, 1999: Interannual (ENSO) and interdecadal (ENSO-like) variability in the Southern Hemisphere tropospheric circulation. *J. Clim.*, **12**, 2113–2123, https://doi.org/10.1175/1520-0442(1999)012⟨2113:IEAIEL⟩2.0.CO;2.

Gebrechorkos, S., S. Hülsmann, and C. Bernhofer, 2019: Long-term trends in rainfall and temperature using high-resolution climate datasets in East Africa. *Sci Rep*, **9 (11376)**, https://doi.org/10.1038/s41598-019-47933-8.

Giannini, A., R. Saravanan, and P. Chang, 2003: Oceanic forcing of Sahel rainfall on interannual to interdecadal time scales. *Science*, **302**, 1027–1030, https://doi.org/10.1126/science.1089357.

Gloor, M., and Coauthors, 2015: Recent Amazon climate as background for possible ongoing and future changes of Amazon humid forests. *Global Biogeochem. Cycles*, **29**, 1384–1399, https://doi.org/10.1002/2014GB005080.

Harris, P., C. Huntingford, and P. Cox, 2008: Amazon Basin climate under global warming: the role of the sea surface temperature. *Phil. Trans. R. Soc. B*, **363**, 1753–1759, https://doi.org/10.1098/rstb.2007.0037.

Hazeleger, W., and Coauthors, 2010: EC-Earth: a seamless earth-system prediction approach in action. *Bull. Amer. Meteor. Soc.*, **91**, 1357–1364, https://doi.org/10.1175/2010BAMS2877.1.

Herger, N., B. M. Sanderson, and R. Knutti, 2015: Improved pattern scaling approaches for the use in climate impact studies. *Geophysical Research Letters*, **42 (9)**, 3486–3494, https://doi.org/https://doi.org/10.1002/2015GL063569.

Hersbach, H., and Coauthors, 2020: The ERA5 global reanalysis. *Q J R Meterol Soc*, **146**, 1999–2049, https://doi.org/10.1002/qj.3803.

Hoerling, M., J. Eischeid, and J. Perlwitz, 2010: Regional precipitation trends: Distinguishing natural variability from anthropogenic forcing. *J. Climate*, **23**, 2131–2145, https://doi.org/10.1175/2009JCLI3420.1.

Huang, B., and Coauthors, 2017: Extended Reconstructed Sea Surface Temperature, version 5 (ERSSTv5): Upgrades, validations, and intercomparisons. *J. Climate*, **30**, 8179–8205, https://doi.org/10.1175/JCLI-D-16-0836.1.

Kay, J., and Coauthors, 2015: The Community Earth System Model (CESM) Large Ensemble Project: A community resource for studying climate change in the presence of internal climate variability. *Bull. Amer. Meteor. Soc.*, **96**, 1333–1349, https://doi.org/10.1175/BAMS-D-13-00255.1.

Kirchmeier-Young, M., F. Zwiers, and N. Gillett, 2017: Attribution of extreme events in Arctic sea ice extent. *J. Climate*, **30**, 553–571, https://doi.org/10.1175/JCLI-D-16-0412.1.

Knight, J. R., C. Folland, and A. Scaife, 2008: Climate impacts of the Atlantic Multidecadal Oscillation. *Geophys. Res. Lett.*, **33**, https://doi.org/10.1029/2006GL026242.

Konapala, G., A. Mishra, Y. Wada, and M. Mann, 2020: Climate change will affect global water availability through compounding changes in seasonal precipitation and evaporation. *Nat Commun*, **11**, 3044, https://doi.org/10.1038/s41467-020-16757-w.

Kravitz, B., C. Lynch, C. Hartin, and B. Bond-Lamberty, 2017: Exploring precipitation pattern scaling methodologies and robustness among CMIP5 models. *Geosci. Model Dev.*, **10**, 1889–1902, https://doi.org/10.5194/gmd-10-1889-2017.

Kravitz, B., and A. Snyder, 2023: Pangeo-enabled ESM pattern scaling (PEEPS): A customizable dataset of emulated Earth System Model output. *PLOS Climate*, **12**, https://doi.org/10.1371/journal.pclm.0000159.

Kuo, Y., H. Kim, and F. Lehner, 2023: Anthropogenic aerosols contribute to the recent decline in precipitation over the U.S. southwest. *Geophysical Research Letters*, **50 (23)**, e2023GL105 389, https://doi.org/https://doi.org/10.1029/2023GL105389.

Kuo, Y., and Coauthors, 2025: Recent southwestern U.S. drought exacerbated by anthropogenic aerosols and tropical ocean warming. *Nat. Geosci.*, **18**, 578–585, https://doi.org/10.1038/s41561-025-01728-x.

Lehner, F., C. Deser, I. Simpson, and L. Terray, 2018: Attributing the U.S. Southwest's recent shift into drier conditions. *Geophys. Res. Lett.*, **45**, 6251–6261, https://doi.org/10.1029/2018GL078312.

Maher, N., and Coauthors, 2019: The Max Planck Institute Grand Ensemble: Enabling the exploration of climate system variability. *JAMES*, **11**, 2050–2069, https://doi.org/10.1029/2019MS001639.

Moreira, R., B. dos Santos, T. Biggs, F. de Sales, and S. Sieber, 2024: Identifying clusters of precipitation for the Brazilian Legal Amazon based on magnitude of trends and its correlation with sea surface temperature. *Sci Rep*, **14**, https://doi.org/10.1038/s41598-024-63583-x.

Olonscheck, D., and Coauthors, 2023: The new Max Planck Institute Grand Ensemble with CMIP6 forcing and high-frequency model output. *JAMES*, **15**, https://doi.org/10.1029/2023MS003790.

Qian, J., B. Viner, S. Noble, D. Werth, J. Wermter, S. Chiswell, and C. Li, 2024: Understanding observed precipitation change and the new climate normal from the perspective of daily weather types in the Southeast United States. *J. Climate*, https://doi.org/10.1175/JCLI-D-23-0367.1.

Qiu, W., M. Collins, A. A. Scaife, and A. Santoso, 2024: Tropical Pacific trends explain the discrepancy between observed and modelled rainfall change over the Americas. *npj Clim. Atmos. Sci.*, **7**, 201, https://doi.org/10.1038/s41612-024-00750-x.

Rodgers, K., and Coauthors, 2021: Ubiquity of human-induced changes in climate variability. *Earth Syst. Dynam.*, **12**, 1393–1411, https://doi.org/doi.org/10.5194/esd-12-1393-2021.

Ropelewski, C., and M. Halpert, 1987: Global and regional scale precipitation patterns associated with the El Niño/Southern Oscillation. *Mon. Wea. Rev.*, **115**, 1606–1626, https://doi.org/10.1175/1520-0493(1987)115⟨1606:GARSPP⟩2.0.CO;2.

Rowell, D. P., B. B. B. Booth, S. E. Nicholson, and P. Good, 2015: Reconciling past and future rainfall trends over East Africa. *J. Climate*, **28**, 9768–9788, https://doi.org/10.1175/JCLI-D-15-0140.1.

Rugenstein, M., J. Bloch-Johnson, J. Gregory, T. Andrews, T. Mauritsen, C. Li, and et al., 2020: Equilibrium climate sensitivity estimated by equilibrating climate models. *Geophys. Res. Lett.*, **47**, https://doi.org/10.1029/2019GL083898.

Schneider, U., S. Hänsel, P. Finger, E. Rustemeier, and M. Ziese, 2022: GPCC full data monthly product version 2022 at 2.5°: Monthly land-surface precipitation from rain-gauges built on GTS-based and historical data. https://doi.org/10.5676/DWD_GPCC/FD_M_V2022_250.

Seager, R., and M. Hoerling, 2014: Atmosphere and ocean origins of North American droughts. *J. Clim*, **27**, 4581–4606, https://doi.org/10.1175/JCLI-D-13-00329.1.

Seager, R., N. Naik, W. Baethgen, A. Robertson, Y. Kushnir, J. Nakamura, and S. Jurburg, 2010: Tropical oceanic causes of interannual to multidecadal precipitation variability in Southeast South America over the past century. *J. Climate*, **23**, 5517–5539, https://doi.org/ /10.1175/2010JCLI3578.1.

Seneviratne, S., T. Corti, E. Davin, M. Hirschi, E. Jaeger, I. Lehner, B. Orlowsky, and A. Teuling, 2010: Investigating soil moisture–climate interactions in a changing climate: A review. *Earth-Sci. Rev.*, **99**, 125–161, https://doi.org/10.1016/j.earscirev.2010.02.004.

Siler, N., C. Proistosescu, and S. Po-Chedley, 2019: Natural variability has slowed the decline in western U.S. snowpack since the 1980s. *Geophys. Res. Lett.*, **46**, 346–355, https://doi.org/ 10.1029/2018GL081080.

Sun, L., M. Alexander, and C. Deser, 2018: Evolution of the global coupled climate response to Arctic sea ice loss during 1990–2090 and its contribution to climate change. *J. Climate*, **31**, 7823–7843, https://doi.org/10.1175/JCLI-D-18-0134.1.

Tatebe, H., and Coauthors, 2019: Description and basic evaluation of simulated mean state, internal variability, and climate sensitivity in MIROC6. *Geosci. Model Dev.*, **12**, 2727–2765, https://doi.org/10.5194/gmd-12-2727-2019.

Taylor, K. E., R. J. Stouffer, and G. A. Meehl, 2012: An overview of CMIP5 and the experiment design. *Bull. Amer. Metero. Soc.*, **93**, 485–498, https://doi.org/https://doi.org/10.1175/ BAMS-D-11-00094.1.

741 Todd, V., and Coauthors, 2025: North Pacific ocean–atmosphere responses to Holocene and
742 future warming drive Southwest US drought. *Nat. Geosci.*, **18**, 646–652, https://doi.org/10.
743 1038/s41561-025-01726-z.

744 Trenberth, K., G. Branstator, D. Karoly, A. Kumar, N. Lau, and C. Ropolewski, 1998: Progress
745 during TOGA in understanding and modeling global teleconnections associated with tropical sea
746 surface temperatures. *J. Geophys. Res.*, **103**, 14,291–14,324, https://doi.org/10.1029/97JC01444.

747 von Salzen, K., and Coauthors, 2013: The Canadian Fourth Generation Atmospheric Global
748 Climate Model (CanAM4). Part I: Representation of Physical Processes. *Atmosphere Ocean*,
749 **51 (1)**, 104–125, https://doi.org/10.1080/07055900.2012.755610.

750 Weltzin, J., and Coauthors, 2003: Assessing the response of terrestrial ecosystems to potential
751 changes in precipitation. *BioScience*, **53**, 941–952, https://doi.org/10.1641/0006-3568(2003)
752 053[0941:ATROTE]2.0.CO;2.

753 Williams, A., B. Cook, and J. Smerdon, 2022: Rapid intensification of the emerging southwestern
754 North American megadrought in 2020–2021. *Nat. Clim. Chang.*, **12**, 232–234, https://doi.org/
755 https://doi.org/10.1038/s41558-022-01290-z.

756 Wills, R., Y. Dong, C. Proistosescu, K. Armour, and D. Battisti, 2022: Systematic climate model
757 biases in the large-scale patterns of recent sea-surface temperature and sea-level pressure change.
758 *Geophys. Res. Lett.*, **49**, https://doi.org/10.1029/2022GL100011.

759 Xie, P., and P. Arkin, 1997: Global precipitation: A 17-year monthly analysis based on gauge
760 observations, satellite estimates, and numerical model outputs. *Bull. Amer. Metero. Soc.*, **78**,
761 2539–2558, https://doi.org/10.1175/1520-0477(1997)078⟨2539:GPAYMA⟩2.0.CO;2.